

Article

The Use of Cognate Cosolvent to Mediate Localized High-Concentration Electrolytes for High-Voltage and Long-Cycling Lithium-Metal Batteries

Ying Hu ^{1,†}, Dandan Wang ^{1,†}, Qijie Yu ¹, Ziyi He ¹, Fengrui Deng ¹, Hao Yan ¹, Tinglu Song ^{2,*} , Jin-Cheng Zheng ^{3,4} and Yang Dai ^{1,*}

¹ Department of Chemical Engineering, Shanghai University, Shangda Road 99, Shanghai 200444, China; huying0821@shu.edu.cn (Y.H.); 1165325229@shu.edu.cn (D.W.); yulij@shu.edu.cn (Q.Y.); hzyy@shu.edu.cn (Z.H.); 793709866@shu.edu.cn (F.D.); hao-yan@shu.edu.cn (H.Y.)

² Experimental Center of Advanced Materials School of Materials Science & Engineering, Beijing Institute of Technology, Beijing 100081, China

³ Department of Physics, Xiamen University, Xiamen 361005, China; jczheng@xmu.edu.cn

⁴ Department of Physics and Department of New Energy Science and Engineering, Xiamen University Malaysia, Sepang 43900, Malaysia

* Correspondence: song@bit.edu.cn (T.S.); dy1982@shu.edu.cn (Y.D.)

† These authors contributed equally to this work.

Abstract: Localized high-concentration electrolytes (LHCEs) are promising systems for improving the high-voltage performance and interfacial stability of lithium-metal batteries (LMBs). Unfortunately, they are always challenged by liquid–liquid phase separation during solution preparation. Further investigation is always required when the prepared electrolyte has encountered liquid–liquid phase separation previously. Here, we propose a “cognate cosolvent” strategy to mediate phase-separated LiBF₄/fluoroethylene carbonate (FEC) | ethyl trifluoroacetate (TFAE) mixtures with ethyl acetate (EA), forming effective LiBF₄/FEC/EA/TFAE-based LHCEs (B-LHCEs). Because of their unique solvation structure, the B-LHCEs exhibit high oxidative stability, facilitating Li⁺ transport. The optimized B-LHCEs help single-crystal LiMn_{0.8}Mn_{0.1}Co_{0.1}O₂/Li batteries form robust interphases, improving interfacial stability. As a result, distinct performance can be obtained (4.5 V, 500 cycles, ~90%, 1400, ~70%; 25 C, 128 mAh g⁻¹, 4.7 V, 500, 82.5%). This work turns the “impossible” into an “effective” high-voltage electrolyte design, transcending the previous paradigms of electrolyte investigation and enriching LHCE preparation research.



Academic Editor: Hirotoshi Yamada

Received: 18 February 2025

Revised: 30 March 2025

Accepted: 10 April 2025

Published: 15 April 2025

Citation: Hu, Y.; Wang, D.; Yu, Q.; He, Z.; Deng, F.; Yan, H.; Song, T.; Zheng, J.-C.; Dai, Y. The Use of Cognate Cosolvent to Mediate Localized High-Concentration Electrolytes for High-Voltage and Long-Cycling Lithium-Metal Batteries. *Batteries* **2025**, *11*, 156. <https://doi.org/10.3390/batteries11040156>

Copyright: © 2025 by the authors. Licensee MDPI, Basel, Switzerland. This article is an open access article distributed under the terms and conditions of the Creative Commons Attribution (CC BY) license (<https://creativecommons.org/licenses/by/4.0/>).

Keywords: localized high-concentration electrolytes; interfacial stability; high voltage; single-crystal Ni-rich layered cathode

1. Introduction

Improving the energy density and longevity of lithium-ion batteries has become an urgent issue in academia and industry [1–5]. However, the mainstream-utilized lithium-ion battery system with a graphite anode is limited by gravimetric energy density (~300 Wh kg⁻¹). For further improvement (>500 Wh kg⁻¹), replacing the graphite anode with a lithium-metal anode coupled with a high-voltage cathode, such as a Ni-rich layered cathode (LiNi_xMn_yCo_{1-x-y}O₂, x ≥ 0.8, Ni-rich NMC), is considered effective for achieving this target [1,2]. On the Ni-rich NMC cathode side, increasing the charging cutoff is regarded as a productive approach to enhancing capacity and energy density (e.g., enabling an about 15–35% capacity enhancement from 4.3 to 4.7 V) [1,2]. However, Ni-rich NMC

cathodes with a high charging voltage suffer from severe interfacial incompatibility when combined with commercial carbonate-based electrolytes, resulting in an unstable generated interphase and parasitic reactions. These interfacial instabilities can cause particle pulverization, phase transition, gas evolution, and transition metal dissolution, which inevitably result in poor cycling performance. Although the use of single-crystal NMC (S-NMC) to replace polycrystal NMC (P-NMC) cathodes can partially suppress particle pulverization, there are still the challenges of limited long-term cycling stability, poor rate performance, and, even worse, structural collapse under a high-voltage cut-off (>4.3 V) [6–9]. For lithium-metal anodes, due to critical interfacial incompatibility with carbonate-based electrolytes, the formation of an unstable interphase, dendrite growth, and parasitic reactions lead to the degradation of anode performance, resulting in fast capacity fading [1,2].

Due to the strong correlation between high-voltage issues and carbonate-based electrolytes, it is essential to investigate new electrolytes that are compatible with both cathodic and anodic interfaces and produce stable interphases. Therefore, high-concentration electrolytes [8,10], localized high-concentration electrolytes (LHCEs) [2,4,11–13], fluorinated carbonate-based electrolytes [14], and cyclic phosphate-based electrolytes [15,16] have been developed. Among the developed electrolytes, LHCEs retain the local solution structure of concentrated electrolytes while reducing viscosity [12]. Built on hydrofluoroethers (HFEs), such as 1,1,2,2-tetrafluoroethyl-2,2,3,3-tetrafluoropropylether (TTE) [17–20] and bis(2,2,2-trifluoroethyl) ether (BTFE) [4,21], LHCEs can significantly improve high-voltage performance and slow down the growth of lithium dendrites, thereby enhancing interfacial stability and cycling performance. However, these HFEs have high density (>1.4 g cm $^{-3}$) and are expensive, reducing the energy density of the corresponding batteries and increasing costs, thus inhibiting their further development [2]. In addition, the long-term cycling performance of HFE-based LHCEs needs to be further improved. LiBF₄ is a salt with great promise for battery applications and has been widely investigated to improve the high-voltage performance of NMC/Li batteries [10,14,22]. Fluoroethylene carbonate (FEC) is regarded as a valuable compound for constructing a passivated interphase for lithium-metal anodes, and it is often selected as the solvent for LHCEs [23]. Ethyl trifluoroacetate (TFAE) possesses high oxidation stability, is inexpensive (being about one-fifth the cost of HFEs), and has low density (1.19 cm $^{-3}$). It could be an excellent dilute solvent for forming LHCEs. Due to their unique properties, LiBF₄/fluorinated ethyl acetate-based systems have been widely discussed. Unfortunately, TFAE is absolutely excluded in this regard since electrolytes with TFAE always encounter liquid–liquid separation or are claimed to be “insoluble” [10,24].

It is well known that it is highly undesirable to have to abandon further investigations when the prepared electrolyte has previously encountered liquid–liquid phase separation. In fact, liquid–liquid-phase-separated mixtures are heterogeneous, meaning that they are not helpful in battery applications. Even worse, the existence of a liquid–liquid interface results in almost no ion transport taking place. Therefore, liquid–liquid phase separation may prevent a large number of solvents/systems with excellent properties from being used as electrolytes for batteries. If a third part (solvent or system) that is miscible with both incompatible parts is added as a phase-bridging agent, this severe problem can be addressed. As shown in Figure 1a, the LiBF₄/FEC | TFAE system exhibits immiscible and liquid–liquid phase separation, is quite inhomogeneous, and is nearly ionically insulated [10,14,23,25]. In such a situation, further exploration should be ceased.

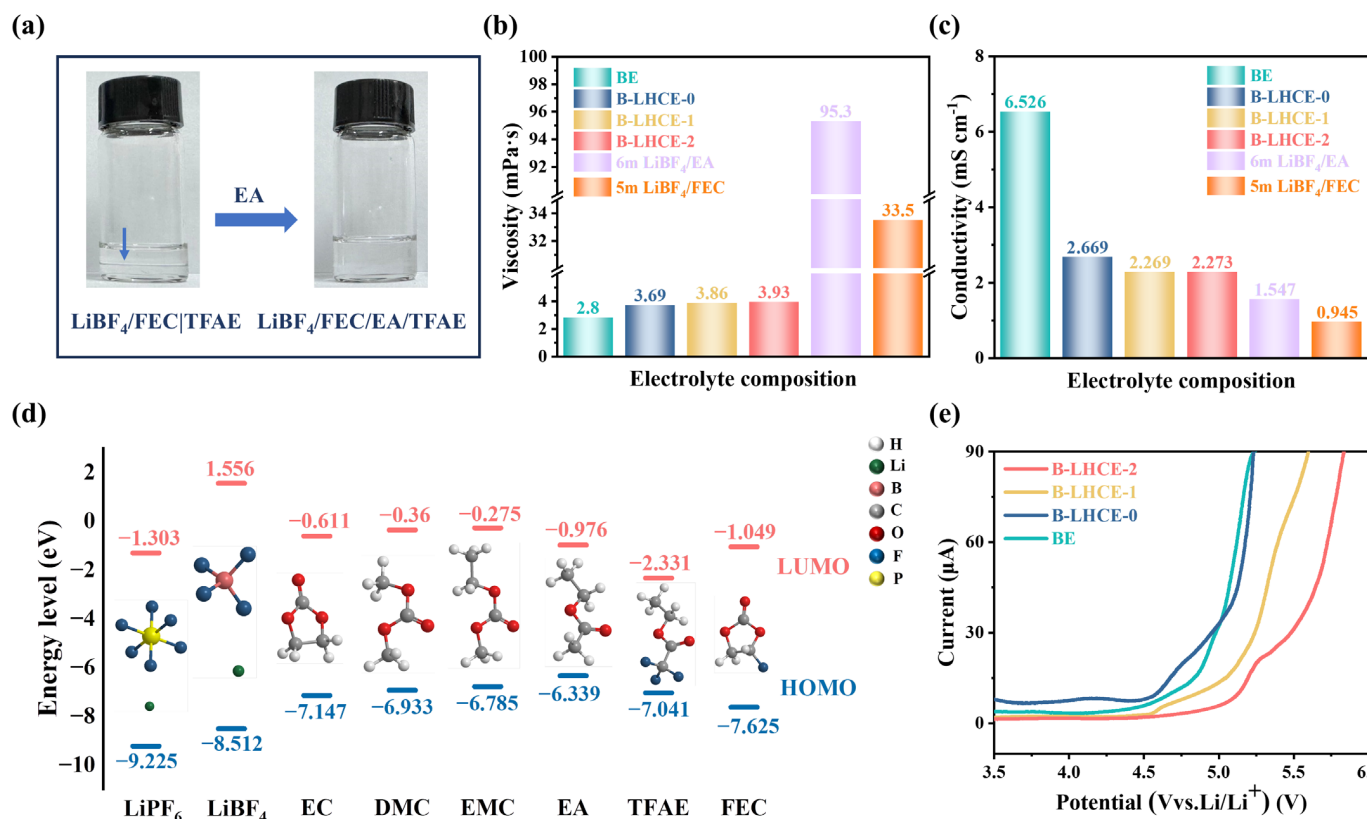


Figure 1. (a) Photos of the formation of B-LHCEs: LiBF₄/FEC | TFAE (1 | 1 v/v) and LiBF₄/FEC/EA/TFAE-based LHCE (1/1/1, v/v/v). (b) Viscosities and (c) ionic conductivities of various electrolytes at 25 °C. (d) Calculated LUMO levels and HOMO levels of the various components for the electrolytes. (e) LSVs of various electrolytes at 25 °C.

To solve this dilemma, we employed the cognate–cosolvent strategy for electrolyte mediation. Ethyl acetate (EA), a cognate solvent with TFAE, is highly miscible with TFAE. It also can be miscible with FEC and dissolve LiBF₄ (Figure 1a and Figure S1). In this work, we used EA to mediate a phase-separated mixture of LiBF₄/FEC | TFAE, forming the homogeneous LiBF₄/FEC/EA/TFAE-based LHCE (Figure 1a), which is easily designable and tailorable. Surprisingly, the mediated LHCEs (B-LHCEs) exhibit high oxidative stability, relatively low viscosities, and high ionic conductivities. Furthermore, the optimized B-LHCE helps both the cathode and anode of the S-NM811/Li batteries to develop robust interphases, thus enhancing interfacial stability under high voltages. Hence, remarkable electrochemical performance of the S-NMC811/Li batteries was observed (4.5 V, 500 cycles, ~90%, 1400 cycles, ~70%; 25 C, 128 mAh g⁻¹, and 4.7 V, 500 cycles, 82.5%). Additionally, due to the unique solvation structure, the B-LHCE facilitates Li⁺-transport, significantly improving the rate capacity. Our work not only provides a potential high-voltage electrolyte system for high-performance Li-metal batteries but also introduces a design strategy that expands the family of LHCEs. More importantly, since liquid–liquid separation is hardly considered in former electrolyte investigations, our work provides a case for making the “impossible” “effective”, revealing new horizons for the paradigm of electrolyte exploration.

2. Materials and Methods

2.1. Electrolyte Preparation

1 M LiPF₆ ethylene carbonate (EC)/dimethyl carbonate (DMC)/ethyl methyl carbonate (EMC) (commercial carbonate-based electrolyte, BE) and lithium tetrafluoroborate (LiBF₄, 99.9%) were purchased from DodoChem (Suzhou, China). Ethyl acetate (EA, 99.5%,

Aladdin, Shanghai, China), ethyl trifluoroacetate (TFAE, 99%, Aladdin), and fluoroethylene carbonate (FEC, 98%, Aladdin) were dried with 4 Å molecular sieves before use. B-LHCEs were prepared by mixing 3 m LiBF₄ molar ratio with FEC/EA/TFAE by volume, similar to what was performed for the reference B-LHCE-0 (3 m LiBF₄ in FEC/EA/TFAE = 1/9/0 v/v/v), B-LHCE-1 (3 m LiBF₄ in FEC/EA/TFAE = 1/7/2 v/v/v), and B-LHCE-2 (3 m LiBF₄ in FEC/EA/TFAE = 1/4/5 v/v/v). The 5 m LiBF₄/FEC and 6 m LiBF₄/EA were prepared by mixing the molar ratio salts with FEC and EA, respectively.

All the electrolyte preparation procedures were carried out in a Mikrouna universal glovebox ($O_2 < 0.1$ ppm, $H_2O < 0.1$ ppm). The viscosity tests were carried out with LC-NDJ-5S (Shanghai, China) in the glovebox. Ionic conductivity was evaluated using electrochemical impedance spectroscopy (EIS) via a Solartron 1260 + 1287 (10 mV, 1 MHz to 0.01 Hz).

2.2. Symmetric Li/Li Cell and Li/Cu Cell

2032-type symmetric Li/separator-electrolyte/Li ($\varphi = 14$ mm) and Li/separator-electrolyte/Cu ($\varphi = 12$ mm) cells were assembled. The long-term plating/stripping test was conducted using a Land CT2001A (Wuhan, China).

2.3. Preparation of NMC811 Cathodes

S-NMC811 (Beijing Easpring Material Technology, Beijing, China), conductive carbon, Super-p, VGCF, and PVDF (80/10/10% in weight) were thoroughly mixed and then stirred in N-Methyl-2-pyrrolidone (NMP) to create a uniform slurry. After that, the slurry was coated on C-coated aluminum foil (Showa Denko Corp., Tokyo, Japan) and then dried at 80 °C for 24 h in a vacuum. The 1C-rate was set as 180 mAh g⁻¹. Then, the dried foil was cut into the resulting coin-shaped electrodes, with an active mass loading of 2–3 mg cm⁻². The 2032-shaped coin cell was assembled with the cathode, separator (Celgard 2400, Celgard, NC, USA), and Li metal in the glovebox. The cycled cathode and lithium metal were carefully dissembled and rinsed with Dimethyl carbonate (DMC) and dried in a glovebox. For high-mass-loading cathodes, the ratio of the S-NMC811 (Beijing Easpring Material Technology) to conductive carbon, Super-p, and VGCF and PVDF was 91/4/5% by weight, with a high active material mass loading of 10–11 mg/cm². The cells were assembled with a thin piece of lithium foil measuring 50 µm. Electrochemical performance was measured using a Land CT2001A operating within 3.0–4.5 V and 3.0–4.7 V, respectively. The EIS was tested using a Solartron 1260 + 1287 (10 mV, 1 MHz to 0.01 Hz) after the various cycles.

3. Results and Discussion

3.1. Physical Properties and Solvation Structures

Figure 1a shows a typical LiBF₄/FEC-EA-TFAE-based LHCE (1/1/1, v/v/v), which is bright and uniform, revealing the miscibility of this system. Because of the high melting point and high viscosity of FEC, we selected 10% FEC by volume, blending it with 90% of various EA/TFAE ratios by volume and 3 m LiBF₄ to form the LHCEs [23]. The B-LHCEs exhibited relatively low viscosities (Figure 1b) and high ionic conductivities (Figure 1c), similar to those of commercial carbonate electrolyte (BE). Although the B-LHCEs possess considerably high concentrations, they still present low viscosities, which can be attributed to the low viscosities of EA/TFAE. The HOMO and LUMO were calculated to assess the electrochemical stability of the solvents and salts, and the results are presented in Figure 1d. Preferentially, electrochemical reduction should be evaluated using the calculated LUMO levels. The low LUMO level of TFAE (−2.331 eV) illustrates that it is easily reduced by lithium, generating the LiF-based SEI. The oxidation priority can be determined by the HOMO level [2]. The low values of the HOMO level for the TFAE (−7.041 eV), LiBF₄

(−8.512 eV), and FEC (−7.625 eV), as well as the localized high concentration, suggest the LiBF₄/FEC-EA-TFAE-based LHCEs have high anti-oxidative capacity. Indeed, these results are further confirmed by the linear sweep voltammetry (LSV) results in Figure 1e. The baseline electrolyte (BE) and the reference electrolyte (B-LHCE-0) decomposed at 4.4 V and 4.5 V, respectively, while the oxidative voltage for the B-LHCEs was significantly increased to 4.7–5.0 V (Figure 1e). The high-decomposition voltage of the B-LHCE is proof of coupling with a high-voltage cathode. Since B-LHCE-2 presented the highest oxidation voltage stability among the B-LHCEs and approached that of the saturated solution (in Figure S1g, LiBF₄ | FEC/EA/TFAE = 1/3/6 v/v/v indicates partial dissolution), B-LHCE-2 was selected as the optimized electrolyte for further electrochemical performance investigation and compared to the carbonate-based electrolyte BE. Also, we tested the Li⁺ transference (t_{Li^+}) numbers for BE and B-LHCE-2 (Figure S1i,j, respectively). B-LHCE-2 possessed a higher t_{Li^+} (0.58) compared to that of BE (0.47), which could compensate for the lower ionic conductivity of B-LHCE-2, facilitating ion transport.

We also employed ab initio molecular dynamics (AIMD) simulations to investigate the solvation structures. Figure 2a–c show simulation snapshots of BE, B-LHCE-0, and B-LHCE-2. Obviously, the LiPF₆ and LiBF₄ salts are homogenous and distributed throughout the solvents in the BE and B-LHCE-0 electrolytes, respectively. In stark contrast, close-packed ion clusters (aggregations) and TFAE as the diluent can be observed in B-LHCE-2, revealing the formation of LHCE [26]. The profiles of the radial distribution function (RDF) at 25 °C are exhibited in Figure 2b,c. The RDFs reveal that the solvation sheath of the comparative sample B-LHCEs-0 (without TFAE) is dominated by EA in its first layer, while B-LHCE-2 (With TFAE) is significantly occupied by FEC in the first solvation shell [27–29]. These results indicate that the addition of TFAE can considerably alter solvation structure, changing the dominant form of the first solvation shell from EA, with a strong solvation power (1.17), to a weak FEC (0.63). Also, the RDF results show that the BE presents a much more powerful solvation EC (1.14) as the dominant coordinated solvent in the first solvation shell.

The RDF profiles also illustrate that the Li⁺ solvation structure in the BE is Li⁺(DMC)_{1.095}(EC)_{1.66}(EMC)_{1.016} (Figure 2d), and the average coordination distances are 1.975 Å (Li–DMC), 2.025 Å (Li–EC), and 1.975 Å (Li–EMC), respectively, while the B-LHCEs-0 (without the TFAE) present Li⁺(FEC)_{0.25}(EA)_{2.26} (Figure 2e) values of 1.975 Å (Li–FEC) and 1.975 Å (Li–EA). Because of the high anti-solvation capability of TFAE, the coordination numbers (CNs) are significantly reduced in B-LHCE-2. In sharp contrast (Figure 2f), B-LHCE-2 displays a Li⁺ solvation structure of Li⁺(FEC)_{0.35}(EA)_{0.87}(TFAE)_{0.40}, with coordination distances of 1.975 Å (Li–FEC), 1.975 Å (Li–EA), and 2.025 Å (Li–TFAE). Enhancing the intensity of Li⁺-anion coordination is considered an alternative effective approach for fabricating weakly solvating electrolytes (WSEs) and generating the anion-derived interphases [22]. The BE presents a coordinated number of 1.09 for Li⁺-PF₆[−], while those for B-LHCEs-0 (Li⁺-BF₄[−]) and B-LHCEs-2 (Li⁺-BF₄[−]) were 2.16 and 2.85, respectively. The increased coordination number of the Li⁺-anion suggests the generation of a WSE for B-LHCEs-2, which may benefit the formation of anion-derived interphases and promote interfacial stability. Therefore, the generation of a weak solvation structure can improve Li⁺ transport and thus improve kinetic capacity [2,22,30,31]. Also, the unique solvation structure can enhance high-voltage stability [11–13]. The solvation structure is further verified by the Raman spectra (Figure 2g). The peak at 766 cm^{−1} was assigned to free BF₄[−]. Blue shifts of the peaks can be observed in the B-LHCEs, revealing the formation of coordinated BF₄[−], contact ion pairs (CIPs), and aggregates (AGGs). The extent of the peak blue shift increases with the increase in TFAE content, indicating that the increase in the TFAE component leads to an increase in concentration. In addition, a broad peak

can be detected at 775 cm^{-1} in B-LHCE-2, which is similar to what was observed for the HCEs (6 m LiBF₄/EA and 5 m LiBF₄/FEC), demonstrating that the concentrated solvation structure was retained after dilution with ‘inert’ TFAE [10,14,22].

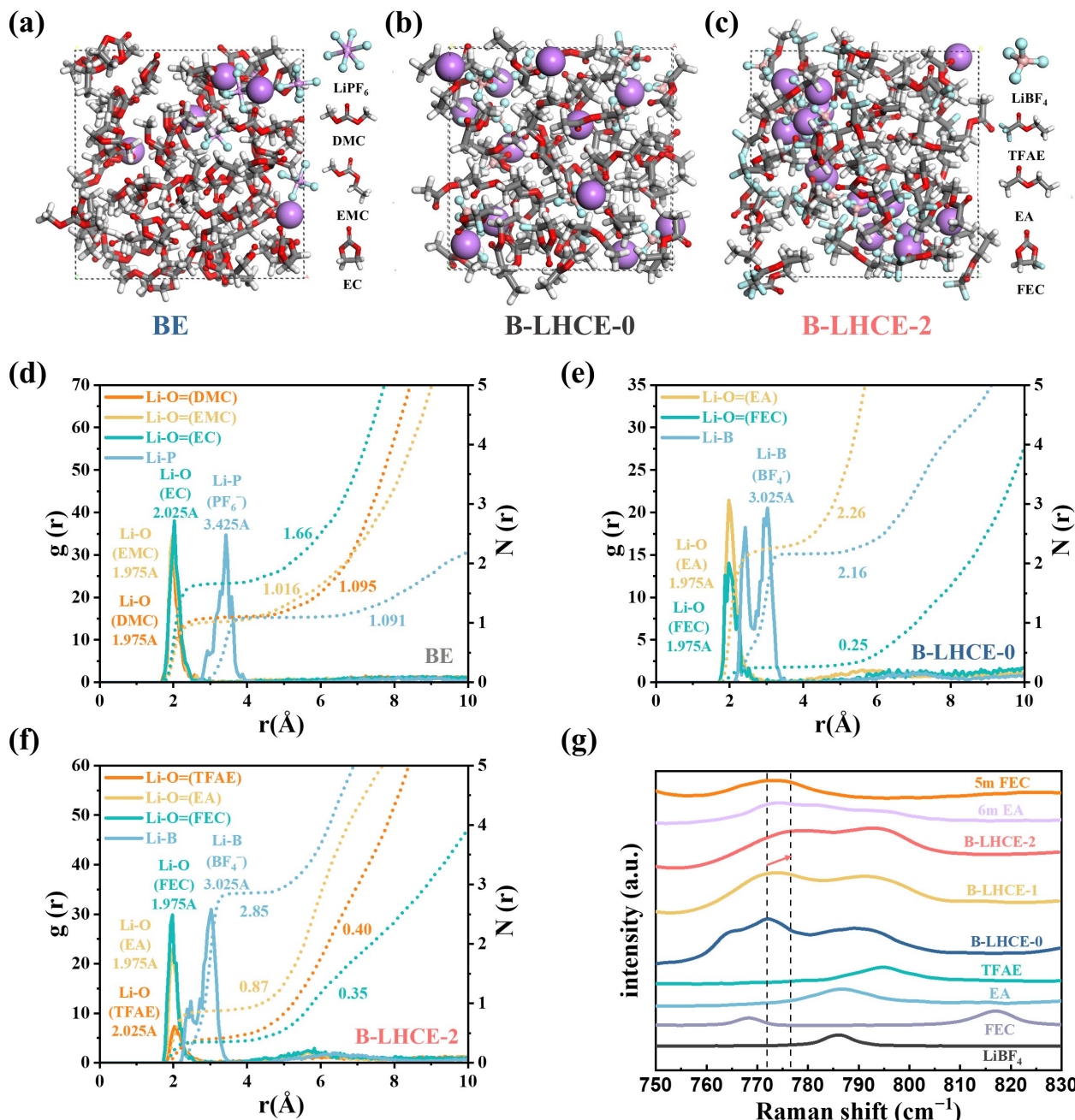


Figure 2. AIMD simulation snapshots of (a) BE, (b) B-LHCE-0, and (c) B-LHCE-2. Radial distribution functions of various components in (d) BE, (e) B-LHCE-0, and (f) B-LHCE-2. (g) Raman spectra of the various components and electrolytes.

The compatibility of a lithium-metal anode/electrolyte is a critical factor in long-term cycling. Figure 3a compares the lithium deposition/stripping profiles for the BE and typical B-LHCE-2 based Li/Li symmetric cells at 0.25 mA cm^{-2} . Superior reversibility with smaller polarization was observed for the B-LHCE-2-based cell compared to that of the BE-based cell, demonstrating uniform and smooth lithium-plating/stripping in the B-LHCE-2-based cell. Moreover, the deposition/stripping process for the BE-based cell terminated at 400 h, while that for the B-LHCE-2-based cell lasted more than 700 h. After

200 h, the cycled lithium anodes were disassembled for further analysis. The Aurbach CE Protocol (Li/Cu cell, Figure 3b,c) was also applied in the evaluation. Similar to the carbonate-based electrolytes [32], the BE-based cell spent most of the Li inventory during several cycles exhibiting abnormal curves and a low CE of 74%. In stark contrast, the B-LHCE-2 based cell exhibited a higher CE of 95.1%. The SEM images (Figure 3d and Figure S2a) reveal that the lithium-anode cycled by BE is significantly deteriorating, with cracking and moss appearance, indicating the highly incompatible interface of the lithium anode/BE. In stark contrast, the anode cycled by B-LHCE-2 exhibits a smooth and dense image (Figure 3e and Figure S2b), corresponding to the Li/Li cycling results, which suggests the generation of a stable interface. The TOF-SIMS (Figure S2c,d and Figure 3f) was also used to investigate the composition and structure of the interphases. The 3D-mapping of typical species, LiF_2^- , $\text{C}_2\text{H}_2\text{O}^-$, and LiBOF_3^- , which originate from LiF; organic species; and the decomposition of LiBF_4 are indicated in Figure 3f, respectively. The LiF-based species and dense layer structure are exhibited in the anode cycled by B-LHCE-2; these features can effectively mitigate the attacks of interfacial parasitic reactions and dendrite growth. Also, the Li-B-O-F layer generated in the SEI can protect the anode. For comparison, the anode cycled by BE possesses few and scattered pieces of LiF with an inhomogeneous distributed interphase, which makes it difficult to prevent dendrite growth and plays a shielding role on the anode [22,33].

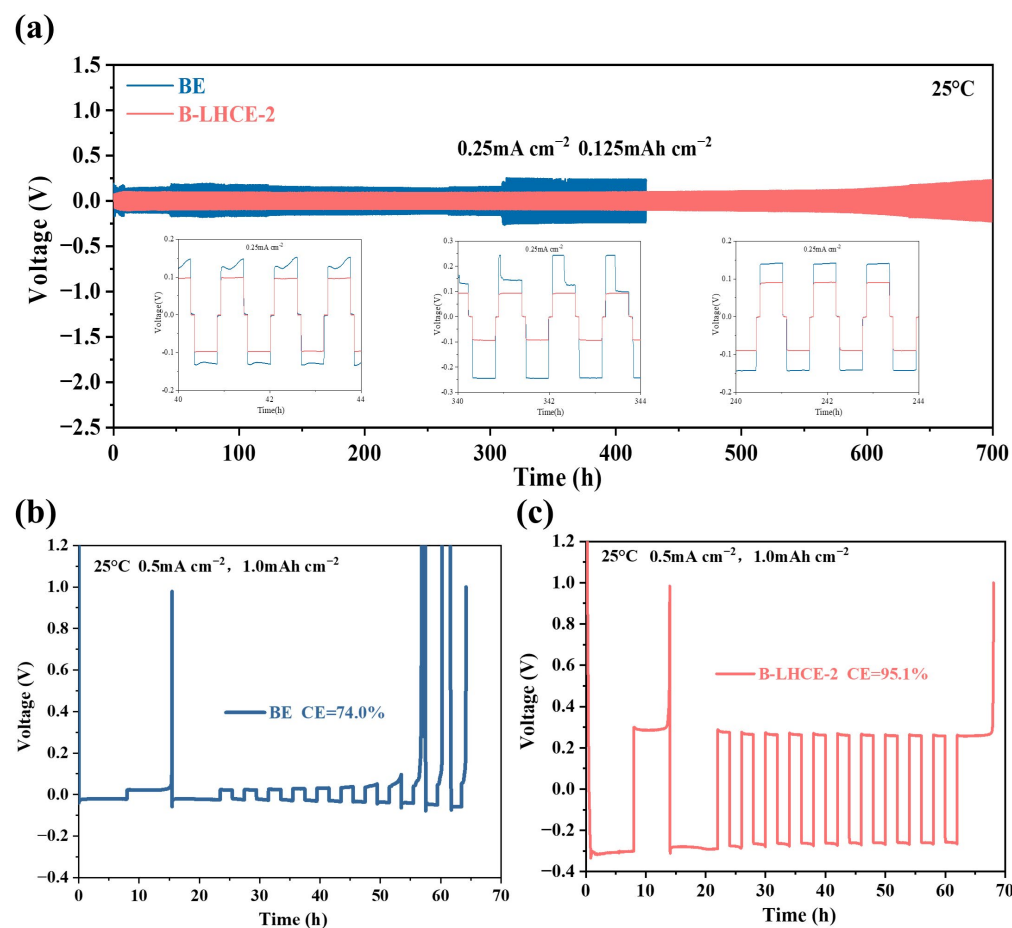


Figure 3. Cont.

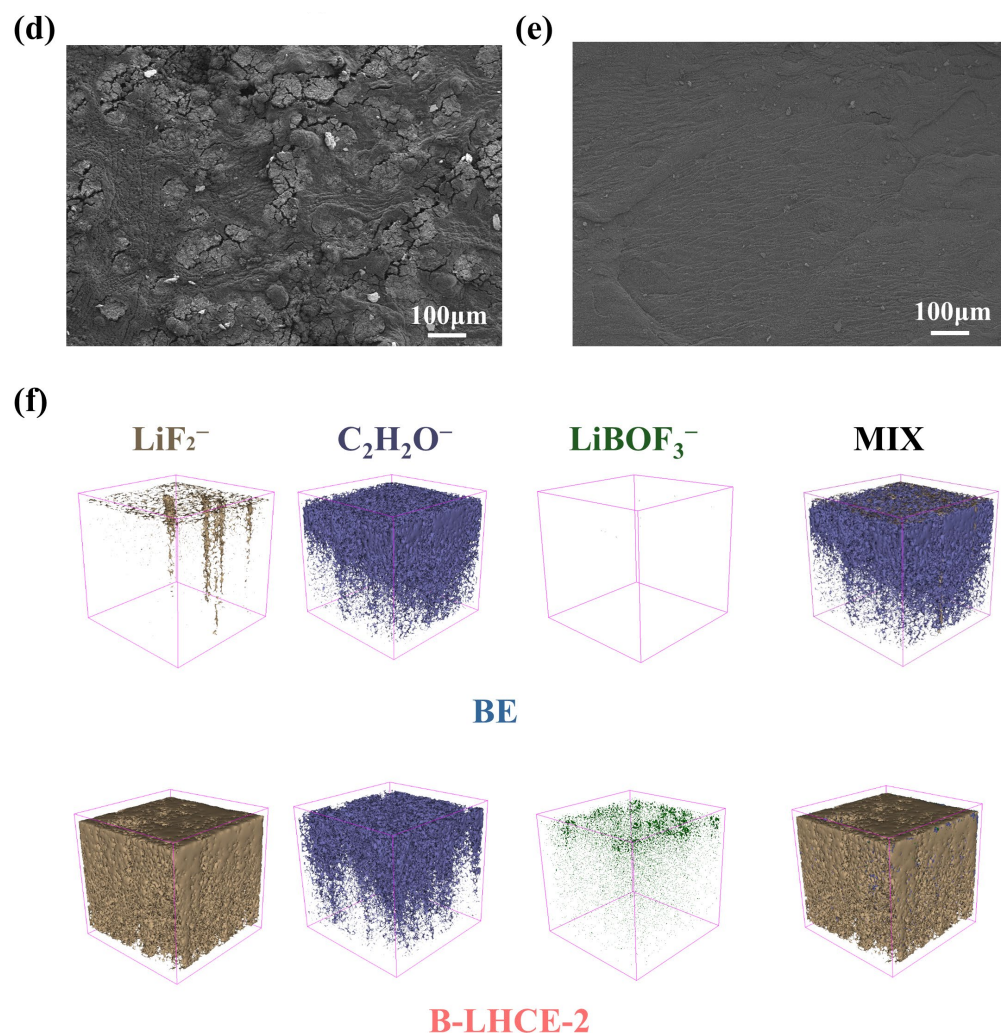


Figure 3. (a) Li/Li symmetric cells with the BE, and B-LHCE-2 electrolytes, cycled at 0.25 mA cm^{-2} . Profiles of the Li/Cu cells examined using the Aurbach test with (b) BE and (c) B-LHCE-2. SEM images of the lithium anodes cycled with (d) BE and (e) B-LHCE-2 electrolytes 200 times. (f) 3D-views of the representative species (TOF-SIMs) for the cycled anodes with BE and B-LHCE-2 electrolytes.

3.2. Battery Performance

Because of its high-voltage stability and excellent compatibility with Li-anodes, B-LHCE was expected to deliver outstanding performance in S-NMC811/Li batteries. Figures 4a and S3a,b compare the rate-performance of the S-NMC811/Li with BE and B-LHCE-2 within 3.0–4.5 V. The battery with B-LHCE-2 presents distinct and low polarized charge–discharge curves even at a high rate of 25 C, demonstrating superb rate capacity. In sharp contrast, the BE shows almost ‘gaping’ curves with an undefined plateau above 3C, indicating severe polarization at high rates and poor rate performance. Also, the rate-cycling curves indicated in Figure 4a highlight the excellent rate capacity of the cell using B-LHCE-2. The cell integrated with B-LHCE-2 displayed a capacity as high as 128.6 mAh g^{-1} even at the ultrahigh rate of 25 C (64.2% for 25 C/0.1 C), showing fast electrochemical kinetics, while the cell cycled with BE barely ran at 25 C, only attaining a capacity retention of 15.4% for 25 C/0.1 C. It is impressive that the B-LHCE-2 possesses relatively lower ionic conductivity and higher viscosity compared to the BE but can deliver such outstanding rate-performance. Thus, the solvation structure plays a critical role in kinetics, aiding in fast-Li⁺ desolvation and greatly improving the rate capability [27,28].

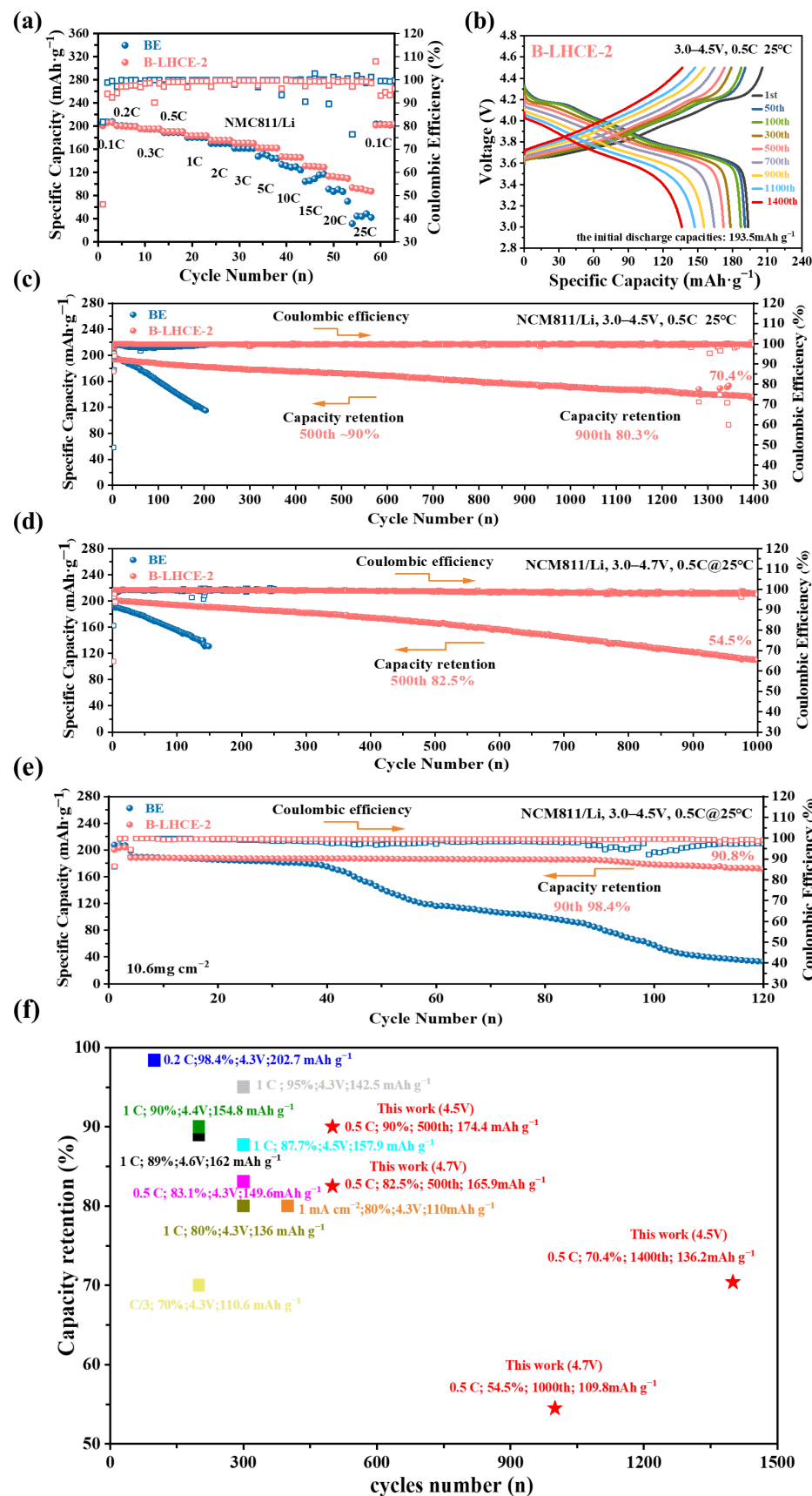


Figure 4. (a) Rate performance of the cells with BE and B-LHCE-2 electrolytes. (b) Charge–discharge profiles of the cell with B-LHCE-2 electrolyte at the various cycles (3.0–4.5 V). Cycling performance of the cells with BE and B-LHCE-2 electrolytes at (c) 3.0–4.5 V and (d) 3.0–4.7 V. (e) Cells assembled with high-mass-loading cathodes (10.6 mg cm^{-2}). (f) Comparison of the results of former reports with this work.

Figure 4b,c and Figure S3c display the cycling performance of S-NMC811/Li with the BE and B-LHCE-2 within 3.0–4.5 V. The cell with B-LHCE-2 had an initial discharge capacity of 193.5 mAh g^{-1} . It showed excellent cycling performance, with a capacity retention of 89.2% after 500 cycles and 70.4% after 1400 cycles. Unfortunately, the BE-based cell underwent a rapid capacity decline within 200 cycles, only delivering a capacity retention of 58.9%.

Also, the charge-discharge profiles of the B-LHCE-2-based cell maintained well-defined shapes even at 1400th cycle, while the profile of the BE-based cell was already highly distorted at the 200th cycle. Furthermore, the S-NMC811/Li with B-LHCE-2 also exhibited an aggressive cutoff of 3.0–4.7 V (Figures 4d and S3d,e). The initial discharge capacity was 201.1 mAh g^{-1} . Capacity retentions of 82.5% and 53% after 500 and 1000 cycles were obtained, respectively, suggesting remarkable high-voltage interfacial stability. The supreme cycling capability of the B-LHCE-2-based cell was attributed to the high voltage stability of the electrolyte and the formation of a durable interphase.

To further investigate the practical application potential, the cells assembled with a high-loading cathode (10.6 mg cm^{-2} , $50 \mu\text{m Li}$) were evaluated (Figures 4e and S3f,g). The B-LHCE-2 cell with an initial discharge capacity of 188.4 mAh g^{-1} exhibited high capacity retention of 90.8% after 120 cycles, while the BE-based cell suffered from rapid capacity attenuation after 40 cycles, with a low-capacity retention of only 25% after 120 cycles. This result highlights the superb performance of the B-LHCE-2 electrolyte in high-voltage applications. Figure 4f and Table S1 show the recently reported high-voltage cycling performance of S-NMC/Li cells [34–39]. It is clear to see that our results are competitive when compared to the former reports, especially in terms of long-term cycling. Furthermore, based on the prices of the agent suppliers, we compared the cost of our B-LHCE-2 electrolyte with that of previously reported high-voltage electrolytes in Table S2. Owing to the large production of the solvents (EA and TFAE), our B-LHCE-2 electrolyte is still competitive in terms of cost. The electrochemical impedance spectra (EIS) were applied for verification, as shown in Figure S4. The cell with B-LHCE-2 presents a small alteration in reaction resistance after the 1st, 100th, and 200th cycles, revealing the generation of stable interphases and interfaces [2]. In contrast, significant variation can be observed for the cell with BE after the 1st, 100th, and 200th cycles, suggesting the formation of unstable interfaces.

Owing to the cathode/electrolyte interface playing essential roles in performance, we further used XRD, SEM, XPS, and TOF-SIMS for investigation. SEM images of the 200 time-cycled S-NMC811 cathodes (3.0–4.5 V) with various electrolytes are depicted in Figure 5a,b. As indicated in Figure 5a, the particles cycled with BE were severely damaged by cracks, and a rough surface can be spotted, which reveals the poorly generated CEI and interface, which hardly prevented the attack on the electrolyte. By comparison, the cathode cycled with B-LHCE-2 exhibits intact particles with a smooth surface (Figure 5b), suggesting that the formed CEI protected the electrode well.

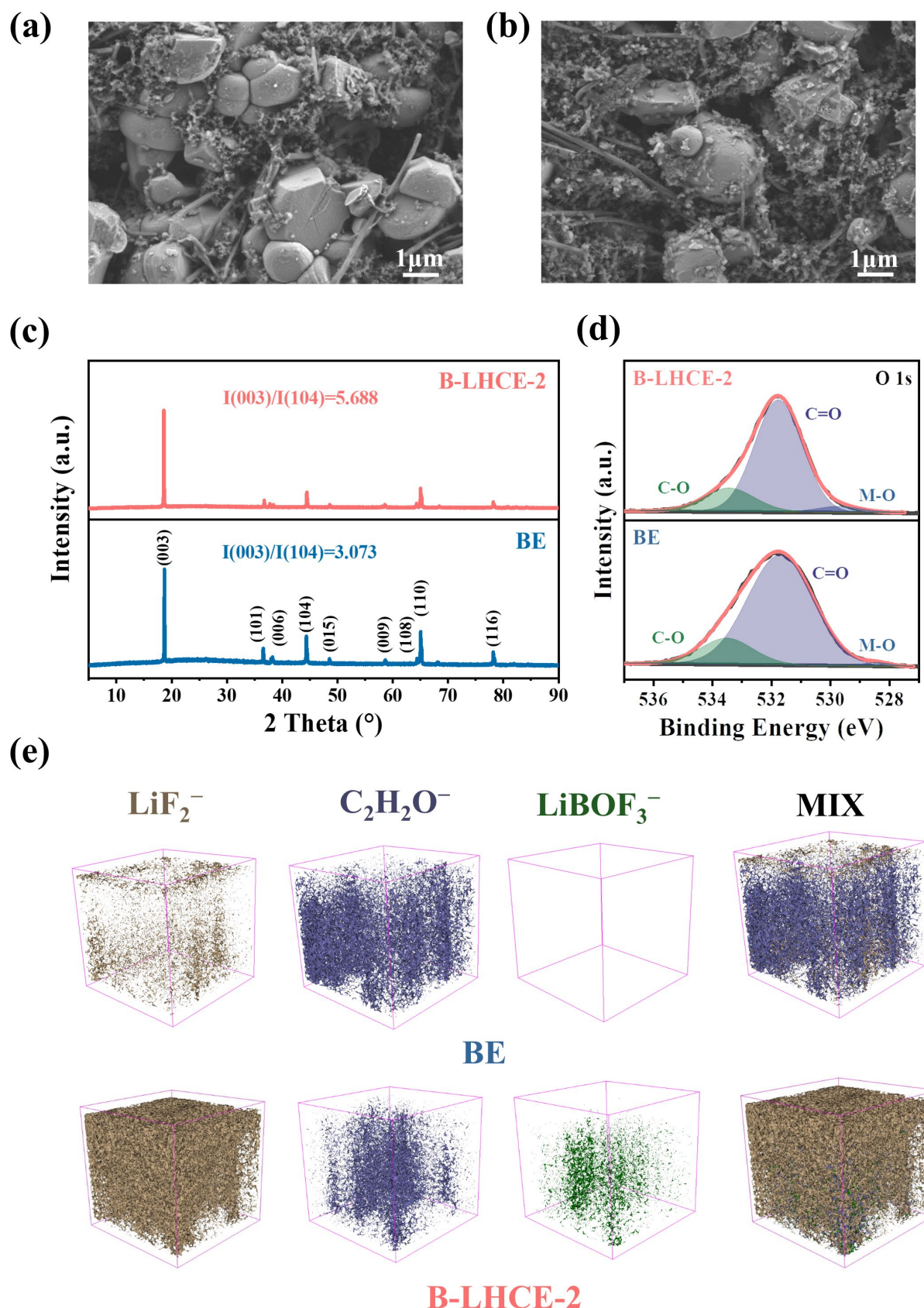


Figure 5. SEM images of the cathodes cycled with (a) BE and (b) B-LHCE-2 electrolytes 200 times. (c) XRD spectra of the cathodes cycled with the various electrolytes. (d) O 1s spectra of the cathodes cycled with various electrolytes. (e) 3D views of the selected species (TOF-SIMs) for the cycled cathodes with BE and B-LHCE-2 electrolytes.

Figure 5c compares the XRD spectra for the electrodes cycled with BE and B-LHCE-2. In the XRD spectra of layered NMC811, the ratio of $I_{(003)}/I_{(104)}$ is always used as an indicator for cation mixing (Figure 5c). The higher the value of the ratio, the lower the degree of cation mixing. In the spectra, the $I_{(003)}/I_{(104)}$ ratio for the cathode cycled with B-LHCE-2 200 times is 5.688, which is significantly larger than that of 3.073 for the BE-based cathode. Also, distinct resolved peak splitting of the (108)/(110) doublets can be detected in cathode cycled with B-LHCE-2, highlighting the protective effect of B-LHCE-2 [16,40]. Therefore, the employment of B-LHCE-2 can maintain bulk structure stability during high-voltage cycling. XPS spectra (Figure S5 and Figure 5d) were applied for further examination. The C1s spectra for both BE and B-LHCE-2-based cathodes can be divided into C-C, C-O, and O-C = O species. Compared to the cathode cycled with BE, weaker peak intensities of C-O can be detected in the cathode cycled with B-LHCE-2, revealing that degeneration can be suppressed [16,40]. In Figure 5d, the intensity of the M-O species (transition metal lattice O^{2-}) in O 1s is associated with the thickness of the formed CEI. The intensity of the M-O species is difficult to observe in the BE-based cathode, suggesting that the generated thick CEI makes the M-O signal (lattice O^{2-}) hard to scrutinize [33,41]. This result can be ascribed to the generation of incompatible interfaces, leading to continuous CEI growth. As a comparison, the M-O species are quite obvious in the cathode cycled with B-LHCE-2, demonstrating the formation of a thin and robust CEI. And in the F1s, the cathode cycled with B-LHCE-2 exhibited a higher quantity of LiF species, which can mitigate the deterioration of the electrolyte. Also, in Figure S5e, the B 1s of the cathode cycled with B-LHCE-2 shows the presence of the B_xO_y species, conforming the contribution of BF_4^- to the formation of CEI [40]. Time-of-flight secondary ion mass spectrometry (TOF-SIMS) depth profiling is a powerful tool for analyzing the chemical composition of the CEI. Figure 5e and Figure S6 compare the depth profiling of typical species of the interphase (CEI) for the cathodes cycled with BE and B-LHCE-2 200 times, respectively. Both interphases contain organic and inorganic substances, and there is no obvious phase separation. The 3D-depth distribution of the species (Figure 5e) reveals that the CEI with B-LHCE-2 has a higher content of LiF-based species and $LiBOF_3^-$ species with a dense layer structure, allowing it to effectively avoid interfacial parasitic reactions. In stark contrast, the CEI created by the BE electrolyte contains more organic species (e.g., $C_2H_2O^-$), which are sparse and have a weaker protective effect on the cathode [22,33].

4. Conclusions

In this work, we provide a ‘cognate-cosolvent’ strategy for mediating the phase-separated mixture to form the uniform B-LHCE. B-LHCE presents relatively low viscosities, high ionic conductivity, high oxidative stability, and a unique weak solvation structure, making it promising for application in high-voltage S-NMC811/Li batteries. Due to the unique solvation structure, B-LHCEs facilitate Li^+ transport and a high rate capacity. F-containing FEC, TFAE, and BF_4^- also form robust SEI and CEI, enhancing the interfacial stability. As a result, excellent electrochemical performance of the S-NMC811/Li batteries was obtained (4.5 V, 500 cycles, ~90%, 1400 cycles, ~70%; 25 C, 128 mAh g⁻¹, and 4.7 V, 500 cycles, 82.5%). This work provides a design strategy for high-performance Li-metal batteries. The simple “cognate solvent” can be applied as a guideline when encountering liquid–liquid phase separation. More significantly, our work also provides a case for “turning waste into treasure”. Because previous electrolyte studies directly ignored liquid–liquid separated mixtures and thus may have excluded many excellent candidates, our work opens a new avenue for revisiting neglected electrolyte systems and breaks new ground in electrolyte exploration.

Supplementary Materials: The following supporting information can be downloaded at <https://www.mdpi.com/article/10.3390/batteries11040156/s1>. Figure S1: Photographic images of the various components: (a) EA/TFAE 1/1 v/v (miscible), (b) EA/FEC 1/1 v/v (miscible), (c) FEC/TFAE 1/1 v/v (miscible), (d) 3 m LiBF₄ | TFAE (dissolvable), (e) 3 m LiBF₄/FEC (completely soluble), (f) 3m LiBF₄/FEC/EA/TFAE 1/7/2 v/v/v (completely soluble) (g) 3 m LiBF₄/FEC/EA/TFAE 1/4/5 v/v/v (completely soluble), (h) 3 m LiBF₄/FEC/EA/TFAE 1/3/6 v/v/v (partially soluble). The DC polarization curve and (inset) electrochemical impedance spectra of the Li symmetric battery with (i) BE (j) B-LHCE-2, respectively. Figure S2: High-magnification SEM images of the lithium anodes cycled with (a) BE, and (b) B-LHCE-2 electrolytes after 200 times. TOF-SIMS depth profiles of the represented species for the cycled lithium anodes in the symmetric cells with (c) BE and (d) B-LHCE-2, respectively. Figure S3: Charge–discharge profiles at various rates of the cells with (a) BE, and (b) B-LHCE-2 electrolytes. Charge–discharge profiles of the cells with (c) BE electrolyte at the various cycles within 3.0–4.5 V, (d) BE electrolyte at the various cycles within 3.0–4.7 V, and (e) B-LHCE-2 electrolyte at the various cycles within 3.0–4.7 V. (f) B-LHCE-2 electrolyte at the various cycles assembled with high mass loading cathodes (10.6 mg cm⁻²), and (g) BE electrolyte at the various cycles assembled with high mass loading cathodes (10.6 mg cm⁻²). Figure S4: EIS spectra of the cells after 1st, 100th, and 200th cycles with (a) BE and (b) B-LHCE-2 electrolytes. Figure S5: XPS spectra of the cycled cathodes: (a) C1s with BE, (b) C1s with B-LHCE-2, (c) F1s with BE, (d) F1s with B-LHCE-2, and (e) B1s with B-LHCE-2. Figure S6: TOF-SIMS depth profiles of the represented species for the cycled S-NMC811cathode with (a) BE and (b) B-LHCE-2, respectively. Table S1: Comparison of the NMC/Li batteries with LHCEs [2,4,20,21,24,34–39]. Table S2: The cost of the B-LHCE-2 compared to the reported high-voltage electrolytes based on the agent suppliers [42–48]

Author Contributions: Y.H.: investigation, formal analysis, and data curation. D.W.: formal analysis and investigation. Q.Y.: date curation and software. Z.H.: formal analysis and investigation. F.D.: formal analysis and investigation. H.Y.: supervision, methodology, and formal analysis. T.S.: validation and formal analysis. J.-C.Z.: validation and formal analysis and writing—reviewing and editing. Y.D.: conceptualization, project administration, supervision, methodology, investigation, and writing—reviewing and editing. All authors have read and agreed to the published version of the manuscript.

Funding: This work was supported by National Natural Science Foundation of China (Grant No. 22209012).

Data Availability Statement: Data are contained within the article or its Supplementary Material.

Acknowledgments: This work is supported by the project of ‘Innovative Research Team of High-level Local Universities in Shanghai’. The authors acknowledge Beijing PARATERA Tech Co., Ltd. for providing HPC resources that have contributed to the research results reported within this paper. URL: <https://cloud.paratera.com/> (accessed on 16 October 2024).

Conflicts of Interest: The authors declare no conflicts of interest.

References

- Xue, W.; Huang, M.; Li, Y.; Zhu, Y.G.; Gao, R.; Xiao, X.; Zhang, W.; Li, S.; Xu, G.; Yu, Y.; et al. Ultra-high-voltage Ni-rich layered cathodes in practical Li metal batteries enabled by a sulfonamide-based electrolyte. *Nat. Energy* **2021**, *6*, 495–505. [[CrossRef](#)]
- He, R.; Deng, K.; Mo, D.; Guan, X.; Hu, Y.; Yang, K.; Yan, Z.; Xie, H. Active Diluent-Anion Synergy Strategy Regulating Nonflammable Electrolytes for High-Efficiency Li Metal Batteries. *Angew. Chem. Int. Ed.* **2024**, *63*, e202317176. [[CrossRef](#)] [[PubMed](#)]
- Doi, T.; Shimizu, Y.; Hashinokuchi, M.; Inaba, M. Dilution of Highly Concentrated LiBF₄/Propylene Carbonate Electrolyte Solution with Fluoroalkyl Ethers for 5-V LiNi_{0.5}Mn_{1.5}O₄ Positive Electrodes. *J. Electrochem. Soc.* **2017**, *164*, A6412–A6416. [[CrossRef](#)]
- Chen, S.R.; Zheng, J.M.; Mei, D.H.; Han, K.S.; Engelhard, M.H.; Zhao, W.G.; Xu, W.; Liu, J.; Zhang, J.G. High-Voltage Lithium-Metal Batteries Enabled by Localized High-Concentration Electrolytes. *Adv. Mater.* **2018**, *30*, 1706102. [[CrossRef](#)] [[PubMed](#)]

5. Chen, K.; Shen, X.; Luo, L.; Chen, H.; Cao, R.; Feng, X.; Chen, W.; Fang, Y.; Cao, Y. Correlating the Solvating Power of Solvents with the Strength of Ion-Dipole Interaction in Electrolytes of Lithium-ion Batteries. *Angew. Chem. Int. Ed.* **2023**, *62*, e202312373. [[CrossRef](#)]
6. Fan, X.; Ou, X.; Zhao, W.; Liu, Y.; Zhang, B.; Zhang, J.; Zou, L.; Seidl, L.; Li, Y.; Hu, G.; et al. In situ inorganic conductive network formation in high-voltage single-crystal Ni-rich cathodes. *Nat. Commun.* **2021**, *12*, 5320. [[CrossRef](#)]
7. Hu, J.; Wang, H.; Xiao, B.; Liu, P.; Huang, T.; Li, Y.; Ren, X.; Zhang, Q.; Liu, J.; Ouyang, X.; et al. Challenges and approaches of single-crystal Ni-rich layered cathodes in lithium batteries. *Natl. Sci. Rev.* **2023**, *10*, nwad252. [[CrossRef](#)]
8. Su, L.; Jarvis, K.; Charalambous, H.; Dolocan, A.; Manthiram, A. Stabilizing High-Nickel Cathodes with High-Voltage Electrolytes. *Adv. Funct. Mater.* **2023**, *33*, 2213675. [[CrossRef](#)]
9. Zhao, W.A.; Wang, K.; Fan, X.M.; Ren, F.C.; Xu, X.Y.; Liu, Y.Y.; Xiong, S.Z.; Liu, X.S.; Zhang, Z.F.; Si, M.Y.; et al. Quantifying Degradation Parameters of Single-Crystalline Ni-Rich Cathodes in Lithium-Ion Batteries. *Angew. Chem. Int. Ed.* **2023**, *62*, e202305281. [[CrossRef](#)]
10. Doi, T.; Fujii, R.; Aoki, Y.; Nagashima, T.; Takehara, K.; Inaba, M. Physicochemical Features of Fluorinated Ethyl Acetate-Based Highly Concentrated Electrolyte Solutions and Their Effects on Electrochemical Properties of $\text{LiNi}_{0.8}\text{Co}_{0.1}\text{Mn}_{0.1}\text{O}_2$ Positive Electrodes. *J. Phys. Chem. C* **2021**, *125*, 12578–12584. [[CrossRef](#)]
11. Zheng, J.; Lochala, J.A.; Kwok, A.; Deng, Z.D.; Xiao, J. Research Progress towards Understanding the Unique Interfaces Between Concentrated Electrolytes and Electrodes for Energy Storage Applications. *Adv. Sci.* **2017**, *4*, 1700032. [[CrossRef](#)]
12. Chen, J.; Zhang, H.; Fang, M.; Ke, C.; Liu, S.; Wang, J. Design of Localized High-Concentration Electrolytes via Donor Number. *ACS Energy Lett.* **2023**, *8*, 1723–1734. [[CrossRef](#)]
13. Cao, X.; Jia, H.; Xu, W.; Zhang, J.-G. Review—Localized High-Concentration Electrolytes for Lithium Batteries. *J. Electrochem. Soc.* **2021**, *168*, 010522. [[CrossRef](#)]
14. Yu, Z.; Yu, W.; Chen, Y.; Mondonico, L.; Xiao, X.; Zheng, Y.; Liu, F.; Hung, S.T.; Cui, Y.; Bao, Z. Tuning Fluorination of Linear Carbonate for Lithium-Ion Batteries. *J. Electrochem. Soc.* **2022**, *169*, 040555. [[CrossRef](#)]
15. Zheng, Q.; Yamada, Y.; Shang, R.; Ko, S.; Lee, Y.-Y.; Kim, K.; Nakamura, E.; Yamada, A. A cyclic phosphate-based battery electrolyte for high voltage and safe operation. *Nat. Energy* **2020**, *5*, 291–298. [[CrossRef](#)]
16. Hou, W.; Zhu, D.; Ma, S.; Yang, W.; Yan, H.; Dai, Y. High-voltage nickel-rich layered cathodes in lithium metal batteries enabled by a sulfolane / fluorinated ether/ fluoroethylene carbonate-based electrolyte design. *J. Power Sources* **2022**, *517*, 230683. [[CrossRef](#)]
17. Ren, X.; Chen, S.; Lee, H.; Mei, D.; Engelhard, M.H.; Burton, S.D.; Zhao, W.; Zheng, J.; Li, Q.; Ding, M.S.; et al. Localized High-Concentration Sulfone Electrolytes for High-Efficiency Lithium-Metal Batteries. *Chem* **2018**, *4*, 1877–1892. [[CrossRef](#)]
18. Lee, S.; Park, K.; Koo, B.; Park, C.; Jang, M.; Lee, H.; Lee, H. Safe, Stable Cycling of Lithium Metal Batteries with Low-Viscosity, Fire-Retardant Locally Concentrated Ionic Liquid Electrolytes. *Adv. Funct. Mater.* **2020**, *30*, 2003132. [[CrossRef](#)]
19. Takada, K.; Yamada, Y.; Yamada, A. Optimized Nonflammable Concentrated Electrolytes by Introducing a Low-Dielectric Diluent. *ACS Appl. Mater. Interfaces* **2019**, *11*, 35770–35776. [[CrossRef](#)]
20. Cao, S.; Wen, F.; Ren, X.; Cao, Y.; Ai, X.; Xu, F. Nonflammable dual-salt localized high-concentration electrolyte for graphite/ $\text{LiNi}_{0.8}\text{Co}_{0.1}\text{Mn}_{0.1}\text{O}_2$ lithium-ion batteries: Li^+ solvation structure and interphase. *J. Power Sources* **2023**, *555*, 232392. [[CrossRef](#)]
21. Yu, L.; Chen, S.; Lee, H.; Zhang, L.; Engelhard, M.H.; Li, Q.; Jiao, S.; Liu, J.; Xu, W.; Zhang, J.-G. A Localized High-Concentration Electrolyte with Optimized Solvents and Lithium Difluoro(oxalate)borate Additive for Stable Lithium Metal Batteries. *ACS Energy Lett.* **2018**, *3*, 2059–2067. [[CrossRef](#)]
22. Jiang, Z.; Mo, J.; Li, C.; Li, H.; Zhang, Q.; Zeng, Z.; Xie, J.; Li, Y. Anion-Regulated Weakly Solvating Electrolytes for High-Voltage Lithium Metal Batteries. *Energy Environ. Mater.* **2022**, *6*, e12440. [[CrossRef](#)]
23. Yoo, D.J.; Liu, Q.; Cohen, O.; Kim, M.; Persson, K.A.; Zhang, Z. Rational Design of Fluorinated Electrolytes for Low Temperature Lithium-Ion Batteries. *Adv. Energy Mater.* **2023**, *13*, 2204182. [[CrossRef](#)]
24. Nagashima, T.; Aoki, Y.; Kimura, K.; Inaba, M.; Doi, T. High-Capacity $\text{LiNi}_{0.8}\text{Co}_{0.1}\text{Mn}_{0.1}\text{O}_2$ Positive-Electrodes in the Nearly Saturated and Fluorinated Acetate-Diluted Electrolyte Solutions. *ACS Appl. Energy Mater.* **2024**, *7*, 2707–2714. [[CrossRef](#)]
25. Bedoch, A.M.; Koga, G.Y.; Nogueira, R.P.; Zepon, G. On the Anomalous Behavior of the Charge Transfer Resistance of the Hydrogen Evolution Reaction at Low Overpotentials and Its Relationship with Hydrogen Absorption in Metals. *J. Phys. Chem. C* **2023**, *127*, 12444–12453. [[CrossRef](#)]
26. Cao, X.; Gao, P.; Ren, X.; Zou, L.; Engelhard, M.H.; Matthews, B.E.; Hu, J.; Niu, C.; Liu, D.; Arey, B.W.; et al. Effects of fluorinated solvents on electrolyte solvation structures and electrode/electrolyte interphases for lithium metal batteries. *Proc. Natl. Acad. Sci. USA* **2021**, *118*, e2020357118. [[CrossRef](#)]
27. Borodin, O.; Olgun, M.; Ganesh, P.; Kent, P.R.; Allen, J.L.; Henderson, W.A. Competitive lithium solvation of linear and cyclic carbonates from quantum chemistry. *Phys. Chem. Chem. Phys.* **2016**, *18*, 164–175. [[CrossRef](#)]
28. Xu, K. *Electrolytes, Interfaces and Interphases*; The Royal Society of Chemistry: London, UK, 2023; p. 471.

29. Su, C.-C.; He, M.; Amine, R.; Rojas, T.; Cheng, L.; Ngo, A.T.; Amine, K. Solvating power series of electrolyte solvents for lithium batteries. *Energy Environ. Sci.* **2019**, *12*, 1249–1254. [[CrossRef](#)]
30. Wang, Q.; Zhao, C.; Wang, J.; Yao, Z.; Wang, S.; Kumar, S.G.H.; Ganapathy, S.; Eustace, S.; Bai, X.; Li, B.; et al. High entropy liquid electrolytes for lithium batteries. *Nat. Commun.* **2023**, *14*, 440. [[CrossRef](#)]
31. Chen, L.; Wang, J.; Chen, M.; Pan, Z.; Ding, Y.; Song, Z.; Ai, X.; Cao, Y.; Chen, Z. “Dragging effect” induced fast desolvation kinetics and -50°C workable high-safe lithium batteries. *Energy Storage Mater.* **2024**, *65*, 103098. [[CrossRef](#)]
32. Liu, Q.; Jiang, W.; Xu, J.; Xu, Y.; Yang, Z.; Yoo, D.-J.; Pupek, K.Z.; Wang, C.; Liu, C.; Xu, K.; et al. A fluorinated cation introduces new interphasial chemistries to enable high-voltage lithium metal batteries. *Nat. Commun.* **2023**, *14*, 3678. [[CrossRef](#)]
33. Dai, Y.; Zhuang, M.; Deng, Y.-X.; Liao, Y.; Gu, J.; Song, T.; Yan, H.; Zheng, J.-C. Stable Cycling of All-Solid-State Lithium Batteries Enabled by Cyano-Molecular Diamond Improved Polymer Electrolytes. *Nano Micro Lett.* **2024**, *16*, 217. [[CrossRef](#)] [[PubMed](#)]
34. Zhu, M.; Jiao, X.; Wang, W.; Chen, H.; Li, F. Localized high-concentration electrolyte enabled by a novel ester diluent for lithium metal batteries. *Chem. Commun.* **2023**, *59*, 712–715. [[CrossRef](#)] [[PubMed](#)]
35. Liu, M.; Li, X.; Zhai, B.; Zeng, Z.; Hu, W.; Lei, S.; Zhang, H.; Cheng, S.; Xie, J. Diluted High-Concentration Electrolyte Based on Phosphate for High-Performance Lithium-Metal Batteries. *Batter. Supercaps* **2022**, *5*, e202100407. [[CrossRef](#)]
36. Li, T.; Li, Y.; Sun, Y.; Qian, Z.; Wang, R. New Insights on the Good Compatibility of Ether-Based Localized High-Concentration Electrolyte with Lithium Metal. *ACS Mater. Lett.* **2021**, *3*, 838–844. [[CrossRef](#)]
37. Cao, Z.; Haruta, M.; Doi, T.; Inaba, M. Dilution Effects of Highly Concentrated LiBF_4/DMC with Fluorinated Esters on Charge/DischARGE Properties of Ni-rich $\text{LiNi}_{0.8}\text{Co}_{0.1}\text{Mn}_{0.1}\text{O}_2$ Positive Electrode. *J. Electrochem. Soc.* **2020**, *167*, 040508. [[CrossRef](#)]
38. Holoubek, J.; Kim, K.; Yin, Y.; Wu, Z.; Liu, H.; Li, M.; Chen, A.; Gao, H.; Cai, G.; Pascal, T.A.; et al. Electrolyte design implications of ion-pairing in low-temperature Li metal batteries. *Energy Environ. Sci.* **2022**, *15*, 1647–1658. [[CrossRef](#)]
39. Lin, S.; Hua, H.; Lai, P.; Zhao, J. A Multifunctional Dual-Salt Localized High-Concentration Electrolyte for Fast Dynamic High-Voltage Lithium Battery in Wide Temperature Range. *Adv. Energy Mater.* **2021**, *11*, 2101775. [[CrossRef](#)]
40. Li, J.; Li, W.; You, Y.; Manthiram, A. Extending the Service Life of High-Ni Layered Oxides by Tuning the Electrode–Electrolyte Interphase. *Adv. Energy Mater.* **2018**, *8*, 1801957. [[CrossRef](#)]
41. Li, Q.; Wang, Y.; Wang, X.; Sun, X.; Zhang, J.N.; Yu, X.; Li, H. Investigations on the Fundamental Process of Cathode Electrolyte Interphase Formation and Evolution of High-Voltage Cathodes. *ACS Appl. Mater. Interfaces* **2020**, *12*, 2319–2326. [[CrossRef](#)]
42. Xia, L.; Lee, S.; Jiang, Y.; Li, S.; Liu, Z.; Yu, L.; Hu, D.; Wang, S.; Liu, Y.; Chen, G.Z. Physicochemical and Electrochemical Properties of 1,1,2,2-Tetrafluoroethyl-2,2,3,3-Tetrafluoropropyl Ether as a Co-Solvent for High-Voltage Lithium-Ion Electrolytes. *ChemElectroChem* **2019**, *6*, 3747–3755. [[CrossRef](#)]
43. Xu, Z.; Deng, K.; Zhou, S.; Mo, D. High-performance lithium metal batteries enabled by fluorinated aromatic diluent assisted nonflammable localized high-concentration electrolytes. *J. Power Sources* **2023**, *559*, 232631. [[CrossRef](#)]
44. Zhao, Q.; Wu, Y.; Yang, Z.; Song, D.; Sun, X.; Wang, C.; Yang, L.; Zhang, Y.; Gao, J.; Ohsaka, T.; et al. A fluorinated electrolyte stabilizing high-voltage graphite/NCM811 batteries with an inorganic-rich electrode-electrolyte interface. *Chem. Eng. J.* **2022**, *440*, 135939. [[CrossRef](#)]
45. Zheng, X.; Liao, Y.; Zhang, Z.; Zhu, J.; Ren, F.; He, H.; Xiang, Y.; Zheng, Y.; Yang, Y. Exploring high-voltage fluorinated carbonate electrolytes for $\text{LiNi}0.5\text{Mn}1.5\text{O}_4$ cathode in Li-ion batteries. *J. Energy Chem.* **2020**, *42*, 62–70. [[CrossRef](#)]
46. Flamme, B.; Świątowska, J.; Haddad, M.; Phansavath, P.; Ratovelomanana-Vidal, V.; Chagnes, A. Sulfone Based-Electrolytes for Lithium-Ion Batteries: Cycling Performances and Passivation Layer Quality of Graphite and $\text{LiNi}_{1/3}\text{Mn}_{1/3}\text{Co}_{1/3}\text{O}_2$ Electrodes. *J. Electrochem. Soc.* **2020**, *167*, 070508. [[CrossRef](#)]
47. Chen, L.; Lu, J.; Wang, Y.; He, P.; Huang, S.; Liu, Y.; Wu, Y.; Cao, G.; Wang, L.; He, X.; et al. Double-salt electrolyte for Li-ion batteries operated at elevated temperatures. *Energy Storage Mater.* **2022**, *49*, 493–501. [[CrossRef](#)]
48. Lu, D.; Xu, G.; Hu, Z.; Cui, Z.; Wang, X.; Li, J.; Huang, L.; Du, X.; Wang, Y.; Ma, J.; et al. Deciphering the Interface of a High-Voltage (5 V-Class) Li-Ion Battery Containing Additive-Assisted Sulfolane-Based Electrolyte. *Small Methods* **2019**, *3*, 1900546. [[CrossRef](#)]

Disclaimer/Publisher’s Note: The statements, opinions and data contained in all publications are solely those of the individual author(s) and contributor(s) and not of MDPI and/or the editor(s). MDPI and/or the editor(s) disclaim responsibility for any injury to people or property resulting from any ideas, methods, instructions or products referred to in the content.